Clays and Clay Minerals, Vol. 65, No. 4, 273–285, 2017.

THE PROPERTIES OF CLAY MINERALS IN SOIL PARTICLES FROM TWO ULTISOLS, CHINA

Zhi Yi Zhang[1], Li Huang[1,*], Fan Liu[1], Ming Kuang Wang[2], Qing Ling Fu[1], and Jun Zhu[1]

[1] Key Laboratory of Arable Land Conservation (Middle and Lower Reaches of Yangtze River), Ministry of Agriculture, Huazhong Agricultural University, Wuhan 430070, China

[2] Department of Agricultural Chemistry, National Taiwan University, Taipei, 10617, Taiwan

Abstract—Soil aggregates consist of sand, silt, and clay size particles. Many of the clay size particles in soils are clay minerals, which actively influence soil behavior. The properties of clay minerals may change significantly as soil particle size decreases to the nanoscale; however, little information is available about these properties for the Ultisols in China. In the present study, the clay mineral components and structural characteristics of four particle-size fractions (*i.e.*, <2000, 450–2000, 100–450, and 25–100 nm) of two Ultisol samples (Ult-1 and Ult-2) were investigated using elemental analysis, X-ray diffraction, Fourier-transform infrared spectroscopy, and thermal analysis. The molar SiO_2 to Al_2O_3 ratios were lower in the nanoscale particle-size fraction (25–100 nm) than in the 450–2000 and <2000 nm fractions. This indicates greater desilicification and allitization of the smaller Ultisol particles. Furthermore, the Fe oxide and Al oxide contents increased and reached a maximum level in the 25–100 nm fraction of the two Ultisols. Goethite was mainly found in the 100–450 nm and 25–100 nm fractions. The dominant clay minerals in the Ultisol 25–100 nm fraction were kaolinite and illite with a small amount of a hydroxy-interlayered mineral in Ult-1 and gibbsite in Ult-2. The kaolinite crystallinity decreased as particle size decreased. The low crystallinity of the kaolinite in the A horizon 25–100 nm fraction was attributed to a reduction in the thickness of coherent scattering domains, as well as to decreases in OH groups and the dimensions of octahedral AlO_6 sheets. A determination of the chemical and mineralogic properties of the different size fractions of the Ultisols is important to understand the desilicification and Al and Fe oxide enrichment mechanisms during soil formation. The significance of these results can help to reveal the nanoscale transformations of clay minerals. Analysis of clay mineral compositions in nanoparticles can provide the additional data needed to understand the adsorption and mobility of nutrients and pollutants.

Key Words—Clay Mineral, Crystallinity, Kaolinite, Mean Crystal Dimension, Nanoparticles, Ultisol.

INTRODUCTION

Clay minerals in soils tend to occur as particles across a wide range of sizes, which range from a few micrometers to nanometers (Meunier, 2006). Clay mineral nanoparticles (<100 nm), which have a high specific surface area, surface defects, and dislocations, are important in the cycling of nutrients and pollutants (Regelink *et al*., 2011; Li *et al*., 2013). With advances in nanotechnology, clay scientists have begun to focus their attention on the properties of the clay minerals in nanoparticles (Li *et al*., 2012; Regelink *et al*., 2013; Assemi *et al*., 2015; He *et al*., 2015; Zhang *et al*., 2016).

Soil nanoparticles are mainly composed of organic and inorganic solid phases. The inorganic fraction of soils usually contains such constituents as phyllosilicate minerals, Fe (oxyhydr)oxides, and other hydroxides and oxides. Li *et al*. (2012) reported the presence of montmorillonite, kaolinite, hematite, corrensite, dickite-2*M*1, and rectorite in natural soil nanoparticles. The composition and properties of inorganic nanoparticles tend to be influenced by particle size (Banfield and Zhang, 2001). Tsao *et al*. (2011) compared the zeolite-A structures in particles of different size and found 366–1625 repetitions of unit cells in 450–2000 nm particles, 81–366 repetitions in 100–450 nm particles, and 20–81 repetitions in 25–100 nm particles. This indicated that the number of unit cells in the coherent stacking domains decreased with decreases in particle size and that the structures transformed from well crystalline to short-range-ordered (SRO) in the smallest particles. Similarly, allophane and imogolite nanoparticles were shown to be X-ray noncrystalline or SRO aluminosilicates with an Al/Si ratio between 1 and 2 (Theng and Yuan, 2008).

Soil Fe (oxyhydr)oxides occur as SRO particles in the 5–100 nm size range. Regelink *et al*. (2013) extracted 1.0–4.7 g kg^{-1} Fe as Fe (oxyhydr)oxide nanoparticles from podzols using pyrophosphate and these Fe (oxyhydr)oxide nanoparticles were 2–20 nm with the maximum abundance around 5 nm.

Climate change can have significant impacts on weathering and soil clay mineralogy (Dahlgren *et al*., 1997; Wilson, 1999). In Chinese Alfisols under warm temperate climatic conditions, the relative abundance of the dominant clay minerals typically identified have been vermiculite, kaolinite, illite, and montmorillonite (Zhang *et al*., 2016). The clay minerals identified in

* E-mail address of corresponding author:
huang_li62@aliyun.com
DOI:10.1346/CCMN.2017.064064

Chinese Ultisols of subtropical zones, however, are generally vermiculite, illite, kaolinite, gibbsite, hematite, and goethite (Jiang *et al*., 2010). Kaolinite forms in an acidic environment as the product of the strong weathering of other clay minerals and is mainly found at low latitude regions with warm and humid environments (Chamley, 1989). Under subtropical and tropical climatic conditions, some recently developed Alfisols and Ultisols are rich in kaolinite, illite, and illite-smectite mixed layer minerals (Melo *et al*., 2001; Kanket *et al*., 2005; He *et al*., 2008).

Ultisols are widespread in the south of China and have a high content of kaolinite and Fe oxides as a result of intense chemical weathering (Huang, 2000; Huang *et al*., 2010). Kaolinite in highly chemically weathered soils usually has a low crystallinity due to a high content of Fe oxides or the presence of interstratified kaolinite minerals.

Previous studies on the composition and crystal properties of soil clay minerals focused mainly on the <2000 nm clay (Melo *et al*., 2001; Kanket *et al*., 2005; Hong *et al*., 2012; Yin *et al*., 2013). Little systematic study has been paid to inorganic soil nanoparticles. Because soil nanoparticles have a complex structure, extracting sufficient quantities for analysis is difficult, the analysis methods are limited, and very little is known about the crystal chemical properties of clay minerals in nanoparticles (Li *et al*., 2012). The aim of the present study was to: (1) investigate the elemental composition of various size particles (<2000, 450−2000, 100−450, and 25−100 nm) in the Ultisols of China; (2) identify the composition and crystallographic properties of the clay minerals in different size soil particles; and (3) explore the transformation of clay minerals in nanoparticles.

MATERIALS AND METHODS

Site description

Two soil samples (Ult-1 and Ult-2) were collected from the A horizons of two soils from southeast China that were classified as Hapludults according to the soil classification system of the USDA Soil Survey Staff (2014). The Ult-1 sample was collected from 0−47 cm of a soil near Tongcheng City (N 29º13′ and E 113º46′) in Hubei Province and the Ult-2 sample was collected from 0−26 cm of a soil near Danzhou City (N 19º27′ and E 109º17′) in Hainan Province. The two sites are about 143 m above sea level and have a mean annual temperature and mean annual precipitation of 16.9−23.5ºC and 1450−1850 mm, respectively (Table 1). The bulk samples of each soil were air-dried at room temperature and ground to pass through 2, 0.85, and 0.15 mm sieves.

Collection of nanoparticles. Organic matter (OM) in the soil samples was removed using hydrogen peroxide (30%). Then, the clay (<2000 nm) fractions were separated from the bulk soil samples using sedimentation according to Stokes' Law calculations. The 450−2000 and 100−450 nm fractions were separated using centrifugation and the nanoscale particle size fraction (25−100 nm) was separated using an automated ultrafiltration device (AUD, Tony Nano-techno, Taiwan) (Tsao *et al*., 2011).

Soil analyses. The pHs of the bulk soils (<2 mm) were measured at a soil to water ratio of 1:2.5, soil texture was determined using the pipette method (Gee and Bauder, 1986), the organic matter content (OM) of the bulk soil samples (<0.15 mm) was determined using the $K_2Cr_2O_7$/H_2SO_4 oxidation method (Nelson and Sommers, 1996), the cation-exchange capacity (CEC) of the bulk soils (<0.85 mm) was determined using the buffered ammonium acetate method (Rhoades, 1982), the exchangeable Ca and Mg were measured using a Varian AA240FS atomic absorption spectrometer (Varian, Palo Alto, California, USA), and the exchangeable K and Na were measured using a Sherwood M410 flame photometer (Sherwood Scientific, Cambridge, UK) (Dohrmann, 2006). Solutions for elemental analyses were produced using the microwave digestion method and 40 mg samples digested in aqua regia (Guaranteed reagent) and hydrofluoric acid (Guaranteed reagent) (US EPA, 1996). Free Fe oxides (Fed) and Al oxides (Ald) were extracted using the dithionite-citrate-bicarbonate (DCB) method (Mehra and Jackson, 1960). X-ray non-crystalline Fe oxide (Feo) and Al oxide (Alo) were extracted using ammonium oxalate solution (Mckeague and Day, 1966). The concentrations of Si, Al, Fe, Ca, Mg, Mn, and Ti in the microwave-digested solutions were determined using a Varian Visata-

Table 1. Soil site information.

Sample	Climate zone	Elevation (m)	Temperature (ºC)	Precipitation (mm/y)	Vegetation	Parent
Ult-1	subtropical	144	16.9	1450	*Pinus massoniana L* and *Taxodium ascendens B*	granite
Ult-2	tropical	143	23.5	1815	*Hevea brasiliensis M* and *Saccharum officinarum L*	granite

https://doi.org/10.1346/CCMN.2017.064064 Published online by Cambridge University Press

MPX inductively coupled plasma-optical emission spectrometer (ICP-OES) (Varian, Palo Alto, California, USA) and K and Na concentrations were measured using a Sherwood Scientific M410 flame photometer (Sherwood Scientific, Cambridge, UK).

Clay minerals in the different size fractions (<2000, 450−2000, 100−450, and 25−100 nm) were identified with oriented and powder samples using a Bruker D8 Advance X-ray diffractometer (XRD) (Bruker, Rheinstetten, Germany) (Jackson, 1979). The different particle-size fractions before and immediately after (20−30 min) treatment with formamide were used to identify halloysite (Churchman *et al*., 1984). The powder samples were examined using X-ray diffraction (XRD) analysis and Cu-Kα radiation (λ = 1.5418 Å) generated at 40 kV and 40 mA. Diffraction patterns were recorded in the range of 2θ = 3 to 65º at a scanning speed of 1º2θ min^{-1}.

The Hughes and Brown index (H&B index), the ratio of the height of the d_{020} reflection peak excluding the background to the d_{131} and d_{003} reflections, was calculated for kaolinite in the soils from the powder XRD patterns (Hughes and Brown, 1979).

The mean crystal dimension (MCD) was calculated from the full width at half maximum height (FWHM) of kaolinite d_{001} using Scherrer's equation (Klug and Alexander, 1974). The average layer number (ALN) was obtained by dividing MCD by the d_{001} values of kaolinite. Scherrer's equation is given by MCD = $K\gamma/(B\cos\theta)$, K is Scherrer's constant (0.89 in this study), B is the FWHM of d_{001}, θ is the diffraction angle, and γ is the X-ray wavelength.

X-ray diffraction patterns of the oriented and powder samples of the 25−100 nm fraction were also recorded using synchrotron XRD, which was performed at 18 keV on the BL14B1 beamline at the Shanghai Synchrotron Radiation Facility (SSRF) of China. The incident X-ray wavelength (λ) was 0.6887 Å and based on Bragg's Law, the d values of the synchrotron radiation were converted into d values of the Cu target (λ = 1.5418 Å) radiation.

Fourier-transform infrared spectra (FTIR) were obtained using a Bruker Vertex-70 (Bruker, Rheinstetten, Germany) infrared spectrometric analyzer (Madejová, 2003). Derivative thermal gravimetric analyses (DTG) were carried out using a Netzsch TG 209C (Netzsch, Freistaat Bayern, Germany) in the temperature range of 30−800ºC. Samples were heated under a 20 mL min^{-1} flux of N_2 gas at a heating rate of 10ºC min^{-1} (Lessovaia *et al*., 2012).

RESULTS

Soil properties

The physical and chemical properties of the samples (Table 2) revealed that the Ult-1 and Ult-2 soils were acidic with a pH of about 5.0, and the OM contents were 5.4 and 15.4 g kg^{-1}, respectively. The CEC was 16.2 $cmol_c$ kg^{-1} in Ult-1 and 3.6 $cmol_c$ kg^{-1} in Ult-2. The concentrations of the dominant exchangeable cations, Ca^{2+} and Mg^{2+}, were lower in Ult-2 than in Ult-1. The textural classes of Ult-1 and Ult-2 were clay loam and clay, respectively.

The SiO_2 contents decreased with a decrease in particle size and were lowest in the 25−100 fraction with 41.9% in Ult-1 and 35.3% in Ult-2 (Table 3). The Al_2O_3 contents were 33.9% in Ult-1 and 39.9% in Ult-2 in the 450−2000 nm fraction and about 38% in Ult-1 and 41% in Ult-2 in the 100−450 nm fraction. The results showed a Si rich character for the 450−2000 nm fraction and an Al rich character for the 25−100 nm fraction. The Fe_2O_3 content was similar to that of Al_2O_3, was lowest in the 450−2000 nm fraction, and reached a maximum level in the 25−100 nm fraction. The Fe_2O_3 contents in the Ult-1 and Ult-2 25−100 nm fraction were 13.5 and 11.4%, respectively. The molar SiO_2 to Al_2O_3 ratios decreased from 2.56 and 1.64 in the Ult-1 and Ult-2 450−2000 nm fractions to 1.89 and 1.42 in the 25−100 nm fractions. The 450−2000 nm fraction was enriched in Si and depleted in Fe and Al, whereas the 25−100 nm fraction was enriched in Al and Fe and depleted in Si.

In the different particle size fractions, the Fed and Ald (free Fe and Al oxide) contents were highest in the 25−100 fraction and lowest in the 450−2000 nm

Table 2. Basic physical and chemical properties of the bulk soils.

Sample	pH	OM[a] (g kg^{-1})	CEC[b] ($cmol_c$ kg^{-1})	Exchangeable cation ($cmol_c$ kg^{-1}) K^+	Na^+	Ca^{2+}	Mg^{2+}	Texture[c]
Ult-1	4.9 (0.3)	5.4 (0.1)	16.2 (0.1)	0.17 (0.00)	0.08 (0.00)	0.80 (0.03)	0.37 (0.01)	CL
Ult-2	5.1 (0.1)	15.4 (0.4)	3.6 (0.1)	0.01 (0.00)	0.02 (0.00)	0.17 (0.03)	0.13 (0.01)	C

[a] OM, organic matter.
[b] CEC, cation exchange capacity.
[c] CL, clay loam; C, clay.
The values in parentheses are the standard deviations.

https://doi.org/10.1346/CCMN.2017.064064 Published online by Cambridge University Press

Table 3. Chemical components in the different particle size fractions.

Sample	Size (nm)	SiO_2	Al_2O_3	Fe_2O_3	CaO	MgO	K_2O	Na_2O	MnO_2	TiO_2	SiO_2/Al_2O_3 Molar ratio[a]
		(%)									
Ult-1	<2000	45.4	36.4	10.0	2.0	0.8	1.5	3.4	0.1	0.6	2.12
		(2.5)[b]	(2.5)	(0.8)	(1.9)	(0.0)	(0.0)	(0.1)	(0.0)	(0.1)	(0.05)
	450−2000	51.2	33.9	7.1	2.0	0.8	1.4	3.0	0.1	0.6	2.56
		(1.2)	(1.2)	(0.3)	(0.3)	(0.0)	(0.1)	(0.1)	(0.0)	(0.0)	(0.13)
	100−450	42.5	38.4	12.5	1.7	0.6	1.0	2.5	0.0	0.7	1.88
		(0.4)	(0.3)	(0.4)	(0.2)	(0.1)	(0.0)	(0.1)	(0.0)	(0.1)	(0.02)
	25−100	41.9	37.6	13.5	1.9	0.8	1.0	2.7	0.1	0.5	1.89
		(0.1)	(0.4)	(0.7)	(0.2)	(0.1)	(0.1)	(0.1)	(0.0)	(0.0)	(0.0)
Ult-2	<2000	43.6	40.0	8.9	0.3	0.1	1.8	1.0	0.1	0.8	1.71
		(3.7)	(2.3)	(0.2)	(0.1)	(1.6)	(0.2)	(0.1)	(0.1)	(0.1)	(0.1)
	450−2000	42.2	39.9	8.0	0.1	0.2	2.7	1.3	0.2	1.4	1.64
		(0.5)	(1.1)	(1.3)	(0.0)	(0.0)	(0.1)	(0.1)	(0.1)	(0.4)	(0.1)
	100−450	37.1	40.6	10.6	0.4	0.2	1.4	1.2	0.2	0.7	1.54
		(0.6)	(0.5)	(1.0)	(0.0)	(0.1)	(0.0)	(0.0)	(0.1)	(0.2)	(0.0)
	25−100	35.3	48.3	11.4	0.5	0.0	1.1	1.9	0.2	0.8	1.42
		(0.2)	(1.6)	(1.5)	(0.3)	(0.0)	(0.1)	(0.2)	(0.0)	(0.3)	(0.1)

[a] Molar ratio of SiO_2 to Al_2O_3.
[b] The values in parentheses are the standard deviations.

fraction (Table 4). The Fed and Ald contents were 58.2 and 9.8 g kg^{-1} in the Ult-1 25−100 fraction and 110.0 and 17.3 g kg^{-1} in the Ult-2 25−100 nm fraction. High Fed and Ald contents usually indicate chemical weathering of silicates and the formation of Fe oxides. Similarly, the Feo and Alo contents were also highest in the 25−100 fraction, except for the Feo content in Ult-1. Additionally, the Fed content was higher than Feo in all particle size fractions. The high Fed content and the low Feo content indicated a high concentration of well-crystalline Fe-oxides (Fed - Feo = well crystalline Fe oxides) (Pai *et al.*, 1999). The crystalline Fe-oxide concentrations ranged from 56.1−99.8 g kg^{-1} in the 25−100 nm fraction to 23.6−44.1 g kg^{-1} in the 450−2000 nm fraction.

Table 4. Extractable Fe and Al contents in the various particle size fractions (g kg^{-1}).

Sample	Size (nm)	Fed[a]	Ald[a]	Feo[b]	Alo[b]	Fed-Feo[c]
Ult-1	<2000	40.5	6.2	3.0	6.7	37.5
		(0.6)[d]	(0.1)	(0.1)	(0.0)	
	450−2000	24.8	4.0	1.2	2.6	23.6
		(0.0)	(0.1)	(0.0)	(0.0)	
	100−450	56.2	8.8	2.8	5.3	53.4
		(1.8)	(0.1)	(0.1)	(0.2)	
	25−100	58.2	9.8	2.1	6.5	56.1
		(1.4)	(0.1)	(0.1)	(0.1)	
Ult-2	<2000	64.2	6.9	8.5	6.5	55.7
		(1.2)	(0.2)	(0.8)	(0.5)	
	450−2000	47.6	4.0	3.5	2.2	44.1
		(0.8)	(0.1)	(0.1)	(0.1)	
	100−450	82.3	7.3	6.4	4.3	75.9
		(0.8)	(0.2)	(1.0)	(0.7)	
	25−100	110.0	17.3	10.2	13.8	99.8
		(1.8)	(0.5)	(1.2)	(0.6)	

[a] Free Fe and Al.
[b] Oxalate extractable Fe and Al.
[c] Crystalline Fe-oxides = Fed - Feo: oxalate-extractable Fe was subtracted from free Fe.
[d] The values in parentheses are the standard deviations.

https://doi.org/10.1346/CCMN.2017.064064 Published online by Cambridge University Press

Oriented and powder X-ray diffraction analyses

X-ray diffractograms of the various particle size fractions (<2000, 450−2000, 100−450, and 25−100 nm) of Ult-1 (Figure 1) revealed that the Mg-saturated and glycerol solvated (Mg-gly) <2000 nm fraction samples were characterized by peaks at 14.1, 10.1, 7.2, 5.1, 4.82, 4.75, 3.57, and 3.34 Å (Figure 1a). The 14.1 Å peak was also identified in the K-saturated 25ºC sample and partly shifted toward 10.1 Å. The 14.1 Å peak completely disappeared after the K-saturated sample was heated at 350ºC, which indicates the presence of vermiculite (trace) and hydroxy-interlayered vermiculite (HIV) (Chiang *et al*., 1999). The 10.1, 5.1, and 3.34 Å peaks remained unchanged after K-saturation and heat treatments, which indicates the presence of illite. The 7.2 and 3.57 Å peaks disappeared after heating to 550ºC, which indicates the presence of kaolinite or halloysite. Because the halloysite component should completely expand immediately after contact with formamide, formamide was used to identify halloysite in the different size fractions of the tested soils (Churchman *et al*., 1984). In the Ult-1 <2000 nm fraction, the 7.2 Å peak did not expand before or after treatment with formamide (Figure 3), which indicates the absence of halloysite. The 4.82 Å peak of the K-saturated sample disappeared after heating to 350ºC, which indicates the presence of gibbsite. Additionally, an unclear peak between 14 and 10 Å was observed in the <2000, 450−2000, and 100−450 nm fraction samples; however, the peak disappeared completely after heating at 350ºC and possibly indicates the presence of illite-HIV.

Similar to those identified in the <2000 nm fraction, the clay mineral components of the 450−2000, 100−450, and 25−100 nm fractions were HIV, illite, and kaolinite (Figures 1b, 1c, 1d, and 3). In addition, the 7.2 Å peak in the synchrotron XRD patterns of the 25−100 nm fractions was asymmetrical with tailing into the 7.2−10.1 Å region, which indicates the possible presence of disordered kaolinite in the Ult-1 nanoparticles. A comparison of the Mg-gly XRD patterns for the different size fractions (450−2000, 100−450, and 25−100 nm) revealed that clay mineral crystallinity varied with particle size. The intensity of the 14.1 Å peak was weakest in the 25−100 nm fraction and the intensities of the illite (10.1, 5.1, and 3.34 Å) and kaolinite (7.2 and 3.57 Å) peaks decreased with decreases in particle size. Similarly, the HIV and illite peaks for the soil 25−100 nm fractions had the highest intensities in the synchrotron XRD patterns (Figure 1e), which indicates that synchrotron XRD was more powerful than conventional XRD for identifying nanometer size clay minerals. With a particle size decrease from 450−2000 to 25−100 nm, the illite 10.1 Å peak gradually changed from a symmetrical peak to a broad weak peak, and the 3.34 Å peak changed from a symmetrical intense peak to an indistinct and weak peak. The kaolinite 7.2 and 3.57 Å XRD peaks in the 25−100 nm fraction became broader and weaker than in the 450−2000 nm fraction after treatment with Mg-gly. This phenomenon showed that illite and kaolinite crystallinity in the Ult-1 25−100 nm fraction was lower than that of the 450−2000 and 100−450 nm fractions.

The X-ray diffractograms of the various size fractions of Ult-2 were similar to those of Ult-1 (Figures 2 and 3). Illite, kaolinite, and gibbsite were present in the different particle-size fractions of Ult-2. The illite and kaolinite XRD peaks for Ult-2 also changed from symmetrical and intense to broad.

Mineralogy of clay minerals by random powder XRD analysis

The 4.16, 2.69, and 2.43 Å peaks of goethite were identified in the <2000 nm fractions of the two soils (Figure 4). The goethite 4.16 and 2.69 Å peaks had a higher intensity in 100−450 nm fraction than in 450−2000 nm fraction. In the Ult-1 25−100 nm fraction, the goethite peak intensities were similar to those of the 100−450 nm size fraction; however, the increase in XRD peak intensities with a decrease in particle size was more obvious in Ult-2 than in Ult-1. This indicates the presence of goethite in the nanoparticle fractions (100−450 and 25−100 nm).

A sharp peak near 1.54 Å and two broad peaks near 1.50 and 1.49 Å were identified in the Ult-1 and Ult-2 450−2000 nm fraction (Figure 4). The peak at 1.54 Å was assigned to quartz because a sharp 3.34 Å quartz peak was identified in the 450−2000 nm fraction. The 1.50 and 1.49 Å peaks were assigned to dioctahedral species with the 1.49 Å peak assigned to kaolinite and the 1.50 Å peak assigned to other dioctahedral minerals (*e.g.* illite or HIV) (Mirabella and Egli, 2003). As particle size decreased, the peak intensities near 1.54 Å decreased and the peak near 1.50 Å disappeared in the nanoparticle 100−450 and 25−100 nm fractions. The results indicated that the major clay minerals in the Ult-1 and Ult-2 soil nanoparticle fractions were dioctahedral.

The kaolinite d_{001} values for the different size fractions varied from 7.191 to 7.238 Å with a median value of 7.203 Å (Table 5). The range in d_{002} values was narrow (3.566−3.574 Å) in comparison to the d_{001} values. As particle size decreased, the FWHM in the Ult-1 and Ult-2 soils increased from 0.526 and 0.532 in the 450−2000 nm fraction to 0.760 and 0.775 in the 25−100 nm fraction, respectively. The MCD and ALN values were about 150 Å and 22 layers in the 450−2000 nm fraction and about 100 Å and 15 layers in the 25−100 nm fraction, respectively. As a result, the two soil 25−100 nm fractions had lower MCD and ALN values, but higher amounts of free and crystalline oxides (Tables 4 and 5). Additionally, the 4.35 and 2.29 Å peaks of kaolinite disappeared in the conventional and the high energy (18 KeV) synchrotron XRD patterns (Figure 4C). Generally, the kaolinite peaks were

https://doi.org/10.1346/CCMN.2017.064064 Published online by Cambridge University Press

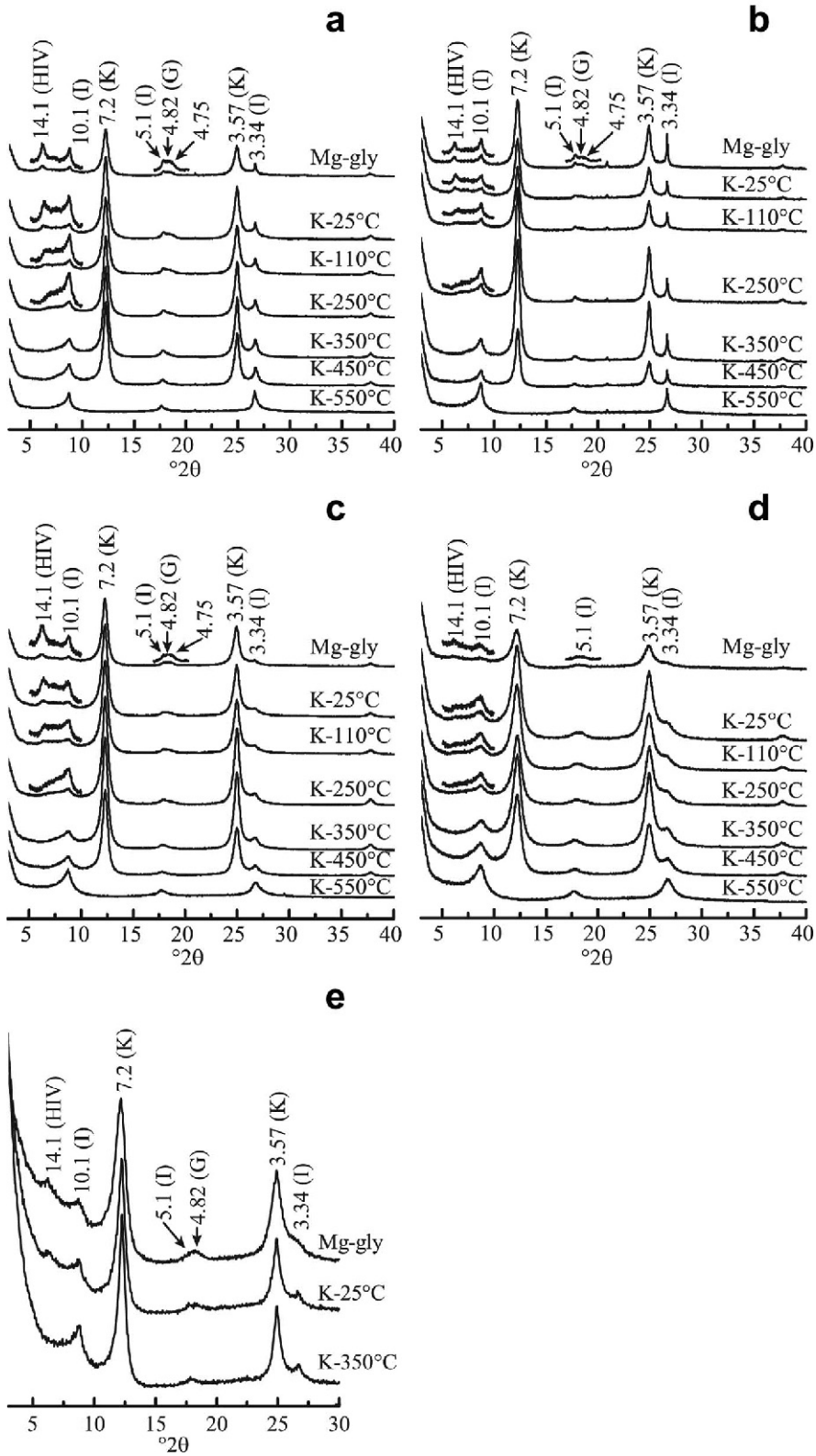

Figure 1. XRD patterns of oriented slides of the different size fractions of Ult-1. Conventional: (a) <2000 nm; (b) 450−2000 nm; (c) 100−450 nm; and (d) 25−100 nm. Synchrotron: (e) 25−100 nm. Abbreviations: HIV = hydroxy-interlayered vermiculite; I = illite; and K = kaolinite. All *d* spacings in Å.

https://doi.org/10.1346/CCMN.2017.064064 Published online by Cambridge University Press

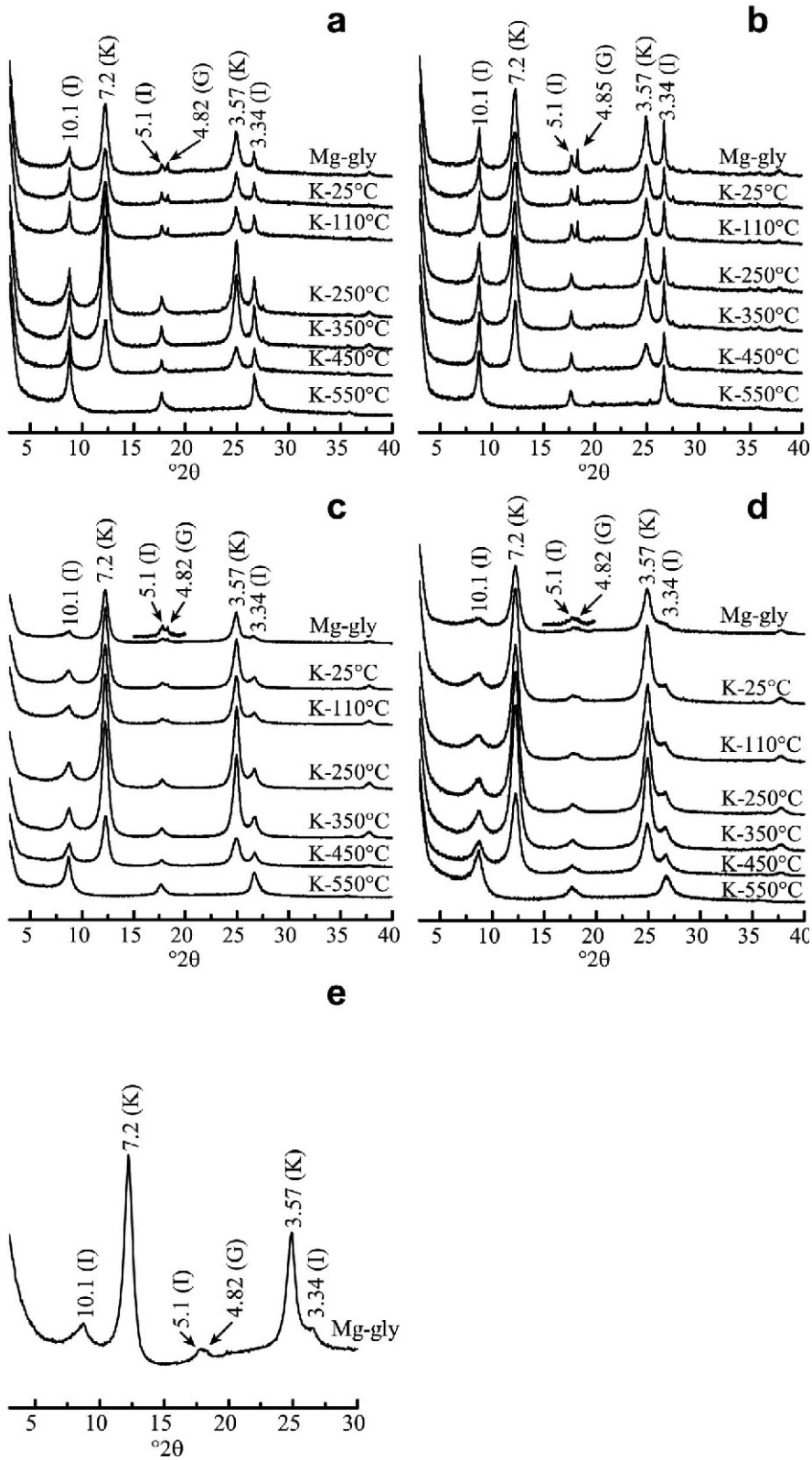

Figure 2. XRD patterns of oriented slides of the different size fractions of Ult-2. Conventional: (a) <2000 nm; (b) 450–2000 nm; (c) 100–450 nm; and (d) 25–100 nm. Synchrotron: (e) 25–100 nm. Abbreviations: I = illite; K = kaolinite; and G = gibbsite. All *d* spacings in Å.

https://doi.org/10.1346/CCMN.2017.064064 Published online by Cambridge University Press

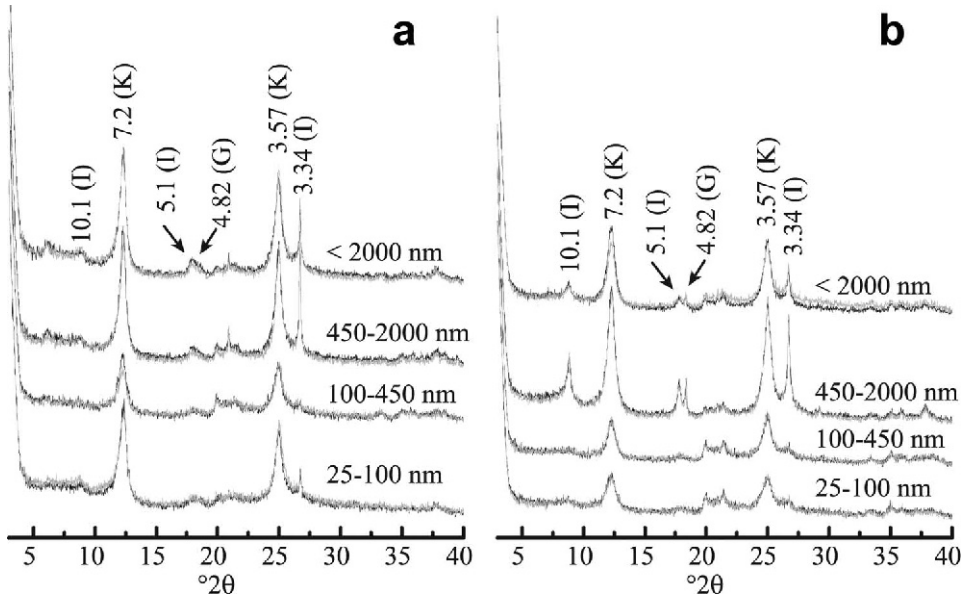

Figure 3. Conventional XRD patterns of different size fractions of (a) Ult-1 and (b) Ult-2 before (black lines) and after (gray lines) formamide (20−30 min) treatment.

classified into three groups: (1) near 4.16 Å ($11\bar{1}$), 4.35 Å ($1\bar{1}0$), and 4.46 Å (020); (2) 2.49 Å (200) and 2.56 Å ($1\bar{3}0$); and (3) the 2.29 Å (131) and 2.34 Å ($1\bar{3}1$) peaks would occur in a moderately disordered kaolinite. The peaks near 2.29−2.34 Å would be absent in highly disordered kaolinite (Wilson, 1987). The disappearance of the 4.35 and 2.29 Å peaks also showed that the kaolinite crystallinity was obviously lower in the 100−450 and 25−100 nm fractions than in the 450-2000 nm fraction. The H&B index varied from 15.0−22.0 and 4.75−15.2 for the various particle-size fractions of Ult-1 and Ult-2, but the lowest H&B index value was observed for the 100−450 and 25−100 nm fractions. The peak kaolinite dehydroxylation temperature for the two soils was approximately 13ºC lower in the 100−450 and 25−100 nm fractions than in the larger particle-size fractions. Melo *et al*. (2001) found a kaolinite dehydroxylation temperature between 489 and 518ºC in highly weathered Ultisols and Alfisols of Brazil and a significant positive relationship was found between the dehydroxylation temperature and the H&B index and MCD. The decrease in dehydroxylation temperature indicated the presence of poorly crystalline kaolinite in the 25−100 nm fraction.

Table 5. Some properties of kaolinite in the various particle size fractions.

Sample	Size (nm)	– *d* value (Å) – 001	002	FWHM[a] (º2θ)	MCD[b] (001) (Å)	ALN[c]	H&B index[d]	PT[e]
Ult-1	<2000	7.203	3.569	0.583	136.2	19.9	15.0	487
	450−2000	7.214	3.568	0.526	151.1	22.0	22.0	487
	100−450	7.238	3.566	0.623	128.0	18.7	17.1	480
	25−100	7.226	3.574	0.760	104.8	15.5	17.0	474
Ult-2	<2000	7.191	3.569	0.586	135.3	19.8	11.0	487
	450−2000	7.200	3.574	0.532	149.2	21.7	15.2	487
	100−450	7.203	3.577	0.638	124.4	18.3	8.7	487
	25−100	7.191	3.566	0.775	102.3	15.2	4.8	474
Mean		7.208	3.570	0.628	128.9	18.9	13.8	487

[a] FWHM, full width at half maximum height of 001 diffraction peak.
[b] MCD, mean crystal dimension along 001 direction.
[c] ALN, average layer number.
[d] H&B index, Hughes and Brown index.
[e] PT, peak temperature of kaolinite and (or) halloysite in the DTG curve, which represents the temperature at the maximum rate of mass change.

https://doi.org/10.1346/CCMN.2017.064064 Published online by Cambridge University Press

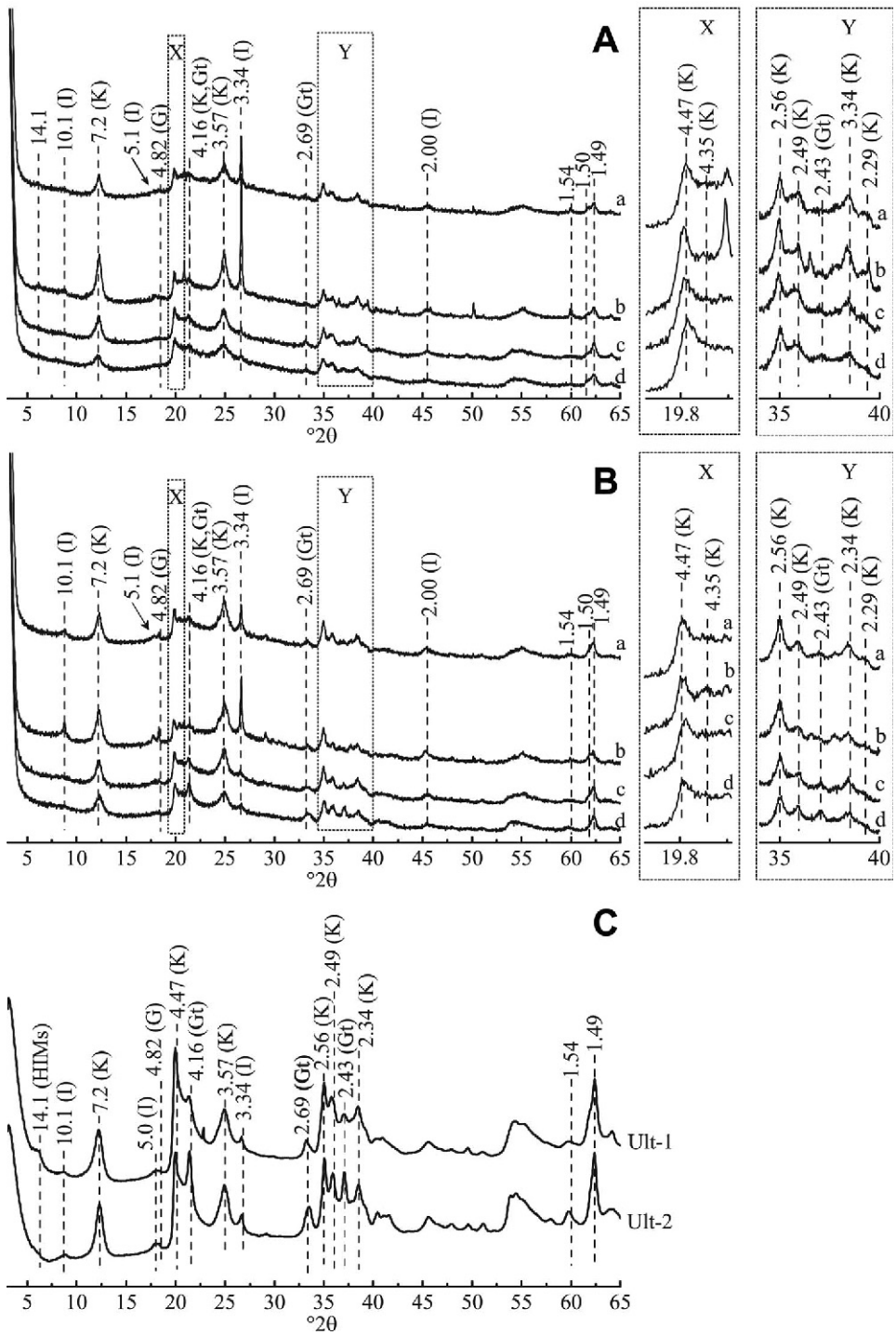

Figure 4. Conventional powder XRD patterns of (A) Ult-1 and (B) Ult-2: (a) <2000 nm, (b) 450–2000 nm, (c) 100–450 nm, and (d) 25–100 nm size fractions with *d* spacings in Å. Synchrotron powder XRD patterns (C) of Ult-1 and Ult-2 25–100 nm fraction. Abbreviations: HIMs = hydroxy-interlayered minerals; I = illite; K = kaolinite; G = gibbsite; Gt = goethite.

Fourier-transform infrared spectroscopy (FTIR) spectra

In the spectra of the two bulk soil samples (<2000 nm fraction), the FTIR stretching bands were observed at 3695, 3652, and 3620 cm^{-1} (Figure 5), which are characteristic of the -OH groups in kaolinite and in dioctahedral 2:1 minerals (Maia *et al*., 2014; Szymański *et al*., 2014). The FTIR stretching vibrations at 3695 and 3652 cm^{-1} originated from the inner surface (outer)

https://doi.org/10.1346/CCMN.2017.064064 Published online by Cambridge University Press

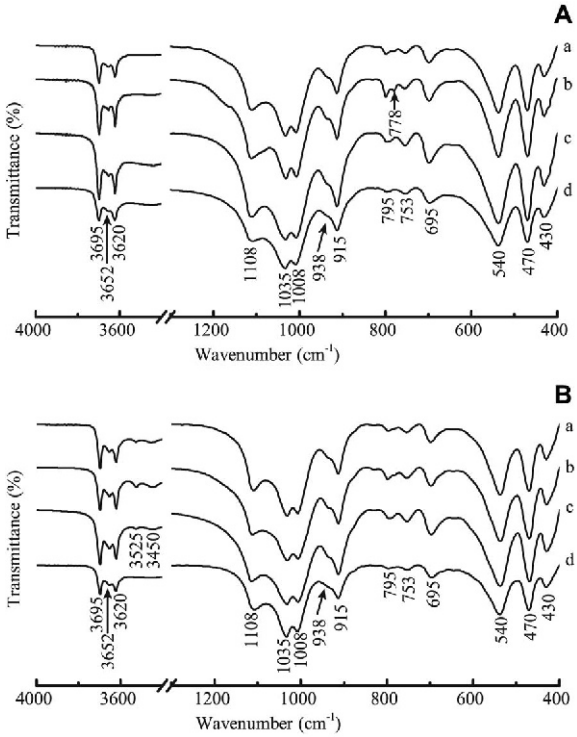

Figure 5. Fourier-transform infrared spectra of Ult-1 (A) and Ult-2 (B) for: (a) <2000 nm; (b) 450−2000 nm; (c) 100−450 nm; and (d) 25−100 nm size fractions.

hydroxyls and the stretching band at 3620 cm^{-1} originated from the inner hydroxyls (Rocha and Klinowski, 1990; Ríos *et al*., 2009). Kaolinite in the clay fraction was also indicated by vibration modes in the Si-O stretching and -OH bending regions (*i.e*., 1115, 1035, 1008, 938, 915, 795, 753, 695, 540, 470, and 430 cm^{-1}) (Eisazadeh *et al*., 2012; Maia *et al*., 2014; Szymański *et al*., 2014). The FTIR vibration modes near 1000−1115 cm^{-1} belonged to the Si-O vibration band and the bands at 938 and 915 cm^{-1} were assigned to the Al-O-H bending modes (Percival *et al*., 1974). In the <2000 nm fraction of Ult-2, the 3525 and 3450 cm^{-1} FTIR stretching modes were also found and indicated the presence of gibbsite (Bardy *et al*., 2007). The gibbsite band could not be observed clearly in the Ult-1 FTIR patterns, however, due to the low gibbsite content.

In the Ult-1 FTIR spectra of the various particle-size fractions (450−2000, 100−450, and 25−100 nm), the kaolinite 3652 cm^{-1} band was symmetrical in the 450−2000 nm fraction, asymmetrical in the 100−450 nm fraction, and in a shoulder stretching mode in the 25−100 nm fraction. In Ult-2, the 3652 cm^{-1} band was asymmetrical for the 450−2000 and 100−450 nm fractions and also changed to a shoulder in the 25−100 nm fraction. As particle size decreased to 25−100 nm, the 3695 and 3620 cm^{-1} stretching bands became weaker than in the other size fractions, which indicates a decrease in the inner and outer -OH groups and kaolinite crystallinity. The low kaolinite crystallinity of the 25−100 nm fraction was also demonstrated by the decreased intensity of the bands at 938, 915, 753, 695, 540, 470, and 430 cm^{-1} as particle size decreased. The 915 and 695 cm^{-1} bands were assigned to the Al-OH vibration (Hu and Yang, 2013) and the intensities of the kaolinite octahedral AlO_6 sheet surface decreased in the 25−100 nm fraction.

DISCUSSION

The clay mineral nanoparticles were generally poorly crystalline or noncrystalline in the Ult-1 and Ult-2 soils. The kaolinite crystallinity further decreased as particle size decreased from 450−2000 nm to 25−100 nm in the two Ultisols (Table 5). A lower kaolinite crystallinity is widespread in strongly weathered Ultisols (Singh and Gilkes, 1992; Melo *et al*., 2001). The presence of interstratified 2:1 clay minerals and the high content of structural Fe are considered to be responsible for the decrease in kaolinite crystallinity (Kanket *et al*., 2005; Huang *et al*., 2012). In the Mg-gly XRD patterns of the two soils, the kaolinite 7.2 Å XRD reflection peak was intense and symmetrical in both the 450−2000 and 100−450 nm fractions, but was asymmetrical in the 25−100 nm fraction with a tail in the high 2θ angle region. The tail of the 7.2 Å peak was clearer in the synchrotron XRD patterns (Figures 1 and 2). The tail phenomenon of the 7.2 Å peak could be caused by many reasons, such as the formation of interstratified kaolinite minerals, halloysite, or a disordered crystallization of kaolinite (Melo *et al*., 2001; Dudek *et al*., 2007). For example, kaolinite was interstratified with smectite or illite in the fine grain size fraction of young acidic soils (Viennet *et al*., 2015; Zhang *et al*., 2016). In the present study, no halloysite was identified using formamide treatment. The 7.2 Å XRD reflection peak remained unchanged, however, after heat treatments at 110, 250, 350, and 450ºC, which indicates the absence of kaolinite interstratified minerals in the two soil 25−100 nm fractions. The poorly crystalline kaolinite must, therefore, have mainly resulted from disordered crystal growth.

In the 25−100 nm soil fractions, the main clay minerals were dominantly illite and disordered kaolinite. The specific surface area of the 25−100 nm fraction was high and the particle size was small (Wada, 1989). Thus, as particle size decreased to the nanoscale, the 25−100 nm fraction clay minerals were subjected to much stronger weathering than the larger particles. Because of the weak molecular attraction between the two crystal layers when the layers overlap in swelling minerals, such as vemiculite and smectite (Fernandez *et al*., 2011), the swelling minerals are more easily influenced by particle size than illite and kaolinite. The main layer types in the 25−100 nm fraction, therefore, were illite and kaolinite and the I-V and I-HIV minerals disappeared (Figures 1 and 2). Viennet *et*

https://doi.org/10.1346/CCMN.2017.064064 Published online by Cambridge University Press

al., (2015) also showed that the layer charge of the expandable layers increased in the coarse fraction of an Alumic Cambisol with randomly interstratified mixed layer minerals. The differences in mineralogy and composition between the coarse clay particles (450−2000 nm) and the 25−100 nm fraction in these Ultisols were important because it partly explains the transformation of clay minerals in soils.

The differences in climate between the Ult-1 and Ult-2 sites (Table 1) also affected the composition of clay minerals in the 25−100 nm fraction. The Ult-1 and Ult-2 soils were in subtropical and tropical climatic areas, respectively. In comparison to the Ult-1 25−100 nm fraction, the Ult-2 25−100 nm fraction was more influenced by climate, as evidenced by strong weathering. Climate has the major role among the various other factors (such as mineralogy and microbial activity) that control weathering processes and has been comprehensively studied (Egli *et al*., 2008; Zhou and Keeling, 2013). In weathering processes, the effect of climate could be regarded as a combination of temperature and rainfall variations (Velde, 1992). A high rainfall region has a more complex clay mineralogy that is dominated by 2:1 clays and kaolinite than a low rainfall region (Deepthy and Balakrishnan, 2005). In the present study, the mean annual temperature and precipitation in Ult-2 (23.5ºC and 1850 mm) were higher than in Ult-1 (16.9ºC and 1450 mm). The HIV in the Ult-1 25−100 nm fraction indicated that in the low OM and moderate acidity environment with frequent drying/wetting cycles, the vermiculite interlayer hydroxyl species persisted as intermediate products of the weathering of 2:1 clay minerals to kaolinite. Ryan *et al*. (2016) studied a tropical soil chronosequence in Costa Rica and found early formed smectite transformed into interstratified kaolinite-smectite (K-S) with 2:1 layers that were increasingly HIV-like and illite-like and that these precursors eventually were altered to kaolinite. In the present study, the 2:1 clay minerals in the 25−100 nm fraction of Ultisols were illlite and HIV. The Ultisols were at the end of an evolution sequence of smectite to kaolinite. The transformation sequence of clay minerals in the Ult-1 25−100 nm fraction in the subtropical zone is summarized as illite→HIV→kaolinite. The Ult-2 25−100 nm fraction was dominated by kaolinite and contained only illite and kaolinite and the disordered kaolinite was the end product of clay mineral transformation. The difference in the clay mineral species in the Ult-1 and Ult-2 soils indicated a zonal distribution of the characteristic clay minerals in the 25−100 nm fraction. Climate was an important factor that determined the kinetics of chemical weathering and mineral transformation in the 25−100 nm fraction. Additionally, when Ultisols are eroded and the finest particles are carried away, a study of the nanoparticle composition could be an important index to understand the erosion process. Goethite is abundant and has the potential to efficiently adsorb anions (*e.g*. nutrients and pollutants) in acidic soil environments.

CONCLUSIONS

The present study indicated that the main clay minerals in the different size fractions of two Ultisols were kaolinite, illite, gibbsite, and a small amount of HIV (and vermiculite) in Ult-1. As soil particle size decreased from 450−2000 to 25−100 nm, the hydroxyl and AlO_6 groups in kaolinite decreased and resulted in a decrease in kaolinite crystallinity in the nanoparticles. The kaolinite MCD, ALN, and PT values were lower in the 25−100 nm particles than in the 450−2000 nm particles. In the two soil 25−100 nm fractions, the MCD and ALN values were about 100 Å and 15 layers/particle, respectively. The endothermic peak temperature was about 474ºC and the H&B indices of kaolinite were 17 and 4.8 for the 25−100 nm fractions of Ult-1 and Ult-2, respectively. Kaolinite crystallinity was lower in the Ult-2 nanoparticles than in the Ult-1 nanoparticles. This study examined the characteristics of clay minerals in soil nanoparticles and provides useful information for further research on nanoscale mineral evolution.

ACKNOWLEDGMENTS

The authors thank the BL14B1 beam line (Shanghai Synchrotron Radiation Facility) for providing the beam time. This research was supported by the National Natural Science Foundation of the People's Republic of China (Grant No. 41271252), and the Fundamental Research Funds for the Central Universities (2013PY002).

REFERENCES

Assemi, S., Sharma, S., Tadjiki, S., Prisbrey, K., Ranville, J., and Miller, J. D. (2015) Effect of surface charge and elemental composition on the swelling and delamination of montmorillonite nanoclays using sedimentation field-flow fractionation and mass spectroscopy. *Clays and Clay Minerals*, **63**, 457−468.

Banfield, J.F. and Zhang, H.Z. (2001) Nanoparticles in the environment. Pp. 1−58 in: *Nanoparticles and the Environment* (J.F. Banfield and A. Navrotsky, editors). Reviews in Mineralogy and Geochemistry, **44**. Mineralogical Society of America and Geochemical Society, Chantilly, Virginia, USA.

Bardy, M., Bonhomme, C., Fritsch, E., Maquet, J., Hajjar, R., Allard, T., Derenne, S., and Calas, G. (2007) Al speciation in tropical podzols of the upper Amazon Basin: a solid-state ^{27}Al MAS and MQMAS NMR study. *Geochimica et Cosmochimica Acta*, **71**, 3211−3222.

Chamley, H. (1989) *Clay Sedimentology*. Springer-Verlag, Berlin, 561 pp.

Chiang, H.C., Wang, M.K., Houng, K.H., White, N., and Dixon, J. (1999) Mineralogy of B horizons in Alpine forest soils of Taiwan. *Soil Science*, **164**, 111−122.

Churchman, G.J., Whitton, J.S., Claridge, G.G.C., and Theng, B.K.G. (1984) Intercalation method using formamide for differentiating halloysite from kaolinite. *Clays and Clay Minerals*, **32**, 241−248.

Dahlgren, R.A., Boettinger, J.L., Huntington, G.L., and Amundson, R.G. (1997) Soil development along an eleva-

tional transect in the western Sierra Nevada, California. *Geoderma*, **78**, 207–236.

Deepthy, R. and Balakrishnan, S. (2005) Climatic control on clay mineral formation: Evidence from weathering profiles developed on either side of the Western Ghats. *Journal of Earth System Science*, **114**, 545–556.

Dohrmann, R. (2006) Problems in CEC determination of calcareous clayey sediments using the ammonium acetate method. *Journal of Plant Nutrition and Soil Science*. **169**, 330–334.

Dudek, T., Cuadros, J., and Huertas, J. (2007) Structure of mixed-layer kaolinite-smectite and smectite-to-kaolinite transformation mechanism from synthesis experiments. *American Mineralogist*, **92**, 179–192.

Egli, M., Mirabella, A., and Sartori, G. (2008) The role of climate and vegetation in weathering and clay mineral formation in late Quaternary soils of the Swiss and Italian Alps. *Geomorphology*, **102**, 307–324.

Eisazadeh, A., Kassim, K.A., and Nur, H. (2012) Solid-state NMR and FTIR studies of lime stabilized montmorillonitic and lateritic clays. *Applied Clay Science*, **67–68**, 5–10.

Fernandez, R., Martirena, F., and Scrivener, K.L. (2011) The origin of the pozzolanic activity of calcined clay minerals: a comparison between kaolinite, illite and montmorillonite. *Cement and Concrete Research*, **41**, 113–122.

Gee, G.W. and Bauder, J.W. (1986) Particle-size analysis. Pp. 383–411 in: *Methods of Soil Analysis*. (A. Klute, editor). Agronomy Monographs, **9**. ASA-SSA, Madison, Wisconsin.

He, Y., Li, D.C., Velde, B., Yang, Y.F., Huang, C.M., Gong, Z.T., and Zhang, G.L., (2008) Clay minerals in a soil chronosequence derived from basalt on Hainan Island, China and its implication for pedogenesis. *Geoderma*, **148**, 206–212.

He, Y., Zeng, F., Lian, Z., Xu, J., and Brookes, P.C. (2015) Natural soil mineral nanoparticles are novel sorbents for pentachlorophenol and phenanthrene removal. *Environmental Pollution*, **205**, 43–51.

Hong, H., Churchman, G.J., Gu, Y., Yin, K., and Wang, C. (2012) Kaolinite-smectite mixed-layer clays in the Jiujiang red soils and their climate significance. *Geoderma*, **173**, 75–83.

Hu, P. and Yang, H. (2013) Insight into the physicochemical aspects of kaolins with different morphologies. *Applied Clay Science*, **74**, 58–65.

Huang, C.Y. (2000) *Soil Science*. China Agriculture Press. Beijing.

Huang, L., Wang, C.Y., Tan, W.F. Hu, H.Q., Cai, C.F., and Wang, M.K. (2010) Distribution of organic matter in aggregates of eroded Ultisols, Central China. *Soil and Tillage Research*, **108**, 59–67.

Huang, P.M., Li, Y., and Sumner, M.E. (2012) *Handbook of Soil Science: Properties and Processes, 2nd ed.*, (M.E. Sumner, editor). CRC Press, Taylor and Francis, Boca Raton, FL.

Hughes, J.C. and Brown, G. (1979) A crystallinity index for soil kaolinite and its relation to parent rock, climate and soil maturity. *European Journal of Soil Science*, **30**, 557–563.

Jackson, M.L. (1979) *Soil Chemical Analysis-Advanced Course, 2nd ed*. Published by the Author, Madison, Wisconsin.

Jiang, J., Xu, R-K., and Zhao, A-Z. (2010) Comparison of the surface chemical properties of four soils derived from Quaternary red earth as related to soil evolution. *Catena*, **80**, 154–161.

Kanket, W., Suddhiprakarn, A., Kheoruenromne, I., and Gilkes, R.J. (2005) Chemical and crystallographic properties of kaolin from Ultisols in Thailand. *Clays and Clay Minerals*, **53**, 478–489.

Klug, H.P. and Alexander, L.E. (1974) *X-ray Diffraction Procedures for Polycrystalline and Amorphous Materials*. New York. Pp. 960.

Lessovaia, S., Dultz, S., Polekhovsky, Y., Krupskaya, V., Vigasina, M., and Melchakova, L. (2012) Rock control of pedogenic clay mineral formation in a shallow soil from serpentinous dunite in the Polar Urals, Russia. *Applied Clay Science*, **64**, 4–11.

Li, W., He, Y., Wu, J., and Xu, J. (2012) Extraction and characterization of natural soil nanoparticles from Chinese soils. *European Journal of Soil Science*, **63**, 754–761.

Li, W., Zhu, X., Yan, H., Xing, B., Xu, J., and Brookes, P.C. (2013) Enhancement of water solubility and mobility of phenanthrene by natural soil nanoparticles. *Environmental Pollution*, **176**, 228–233.

Madejová, J. (2003) FTIR techniques in clay mineral studies. *Vibrational Spectroscopy*, **31**, 1–10.

Maia, A.B., Angélica, R.S., Neves, R.F., Pöllmann, H., Straub, C., and Saalwächter, K. (2014) Use of ^{29}Si and ^{27}Al MAS NMR to study thermal activation of kaolinites from Brazilian Amazon kaolin wastes. *Applied Clay Science*, **87**, 189–196.

Mckeague, J.A. and Day, J.H. (1966) Dithionite and oxalate-extractable Fe and Al as aids in differentiating various classes of soils. *Canadian Journal of Soil Science*, **46**, 13–22.

Mehra, O.P. and Jackson, M.L. (1960) Iron oxide removal from soils and clays by a dithionite-citrate system buffered with sodium bicarbonate. *Clays and Clay Minerals*, **7**, 317–327.

Melo, V.F.,Singh, B., Schaefer, C.E.G.R., Novais, R.F., and Fontes, M.P.F. (2001) Chemical and mineralogical properties of kaolinite-rich Brazilian soils. *Soil Science Society of America Journal*, **65**, 1324–1333.

Meunier, A. (2006) Why are clay minerals small? *Clay Minerals*, **41**, 551–566.

Mirabella, A. and Egli, M. (2003) Structural transformations of clay minerals in soils of a climosequence in an Italian alpine environment. *Clays and Clay Minerals*, **51**, 264–278.

Nelson, D.W. and Sommers, L.E. (1996) Total carbon, organic carbon, and organic matter. Pp. 961–1010 in: *Methods of Soil Analysis. Part 3. Chemical Methods. No. 5* (D.L. Sparks, editor). ASA and SSSA, Madison, Wisconsin.

Pai, C.W., Wang, M.K., and Houng, W.K.H. (1999) Smectites in iron-rich calcareous soil and black soils of Taiwan. *Clays and Clay Minerals*, **47**, 389–398.

Percival, H.J., Duncan, J.F., and Foster, P.K. (1974) Interpretation of the kaolinite-mullite reaction sequence from infrared absorption spectra. *Journal of the American Ceramic Society*, **57**, 57–61.

Regelink, I.C., Weng, L., and Riemsdijk, W.H.V. (2011) The contribution of organic and mineral colloidal nanoparticles to element transport in a podzol soil. *Applied Geochemistry*, **26**, S241–S244.

Regelink, I.C., Weng, L., Koopmans, G.F., and Riemsdijk, W.H.V. (2013) Asymmetric flow field-flow fractionation as a new approach to analyse iron-(hydr)oxide nanoparticles in soil extracts. *Geoderma*, **202**, 134–141.

Rhoades, J.D. (1982) Cation exchange capacity. Pp. 149–157 in: *Methods of Soil Analysis, part 2, 2nd ed.* (A.L. Page, editor). ASA and SSSA, Madison, Wisconsin.

Ríos, C.A., Williams, C.D., and Fullen, M.A. (2009) Nucleation and growth history of zeolite LTA synthesized from kaolinite by two different methods. *Applied Clay Science*, **42**, 446–454.

Rocha, J. and Klinowski, J. (1990) ^{29}Si and ^{27}Al magic-angle-spinning NMR studies of the thermal transformation of kaolinite. *Physics and Chemistry of Minerals*, **17**, 179–186.

Ryan, P.C., Huertas, F.J., Hobbs, F.C., and Pincus, L.N. (2016) Kaolinite and halloysite derived from sequential transformation of pedogenic smectite and kaolinite-smectite in a

120 ka tropical soil chronosequence. *Clays and Clay Minerals*, **64**, 488–516.

Singh, B. and Gilkes, R.J. (1992) Properties of soil kaolinites from south-western Australia. *Journal of Soil Science*, **43**, 645–667.

Szymański, W., Skiba, M., Nikorych, V.A., and Kuligiewicz, A. (2014) Nature and formation of interlayer fillings in clay minerals in Albeluvisols from the Carpathian Foothills, Poland. *Geoderma*, **235**–**236**, 396–409.

Theng, B.K.G. and Yuan, G. (2008) Nanoparticles in the soil environment. *Elements*, **4**, 395–399.

Tsao, T.M., Chen, Y.M., and Wang, M.K. (2011) Origin, separation and identification of environmental nanoparticles: a review. *Journal of Environmental Monitoring*, **13**, 1156–1163.

US EPA. (1996) *Microwave Assisted Acid Digestion of Siliceous and Organically Based Matrices. Method 3052, EPA SW-846, Ch 3.2*. United States Environmental Protection Agency, Washington, DC.

USDA Soil Survey Staff. (2014) *Keys to Soil Taxonomy, 12th ed*. United States Department of Agriculture, Washington, D.C.

Velde, B. (1992) *Introduction to Clay Minerals: Chemistry, Origin, Uses and Environmental Significance* Springer, London.

Viennet, J.C., Hubert, F., Ferrage, E., Tertre, E., Legout, A., and Turpault, M.P. (2015) Investigation of clay mineralogy in a temperate acidic soil of a forest using X-ray diffraction profile modeling: Beyond the HIS and HIV description. *Geoderma*, **241**–**242**, 75–86.

Wada, K. (1989) Allophane and Imogolite. Pp. 1051–1087 in: *Minerals in Soil Environments* (J.B. Dixon and S.B.Weed, editors). Soil Science Society of America, Madison, Wisconsin.

Wilson, M.J. (1987) *A Handbook of Determinative Methods in Clay Mineralogy*. Blackie, New York. 308 pp.

Yin, K., Hong, H., Churchman, G.J., Li, R., Li, Z., Wang, C., and Han, W. (2013) Hydroxy-interlayered vermiculite genesis in Jiujiang late-Pleistocene red earth sediments and significance to climate. *Applied Clay Science*, **74**, 20–27.

Zhang, Z.Y., Huang, L., Liu, F., Wang, M.K. Fu, Q.L., and Zhu, J. (2016) Characteristics of clay minerals in soil particles of two Alfisols in China. *Applied Clay Science*, **120**, 51–60.

Zhou, C.H. and Keeling, J. (2013) Fundamental and applied research on clay minerals: From climate and environment to nanotechnology. *Applied Clay Science*, **74**, 3–9.

(*Received 18 July 2016; revised 11 September 2017; Ms. 1119; AE: P. Ryan*)